THESIS FOR THE DEGREE OF LICENTIATE OF ENGINEERING

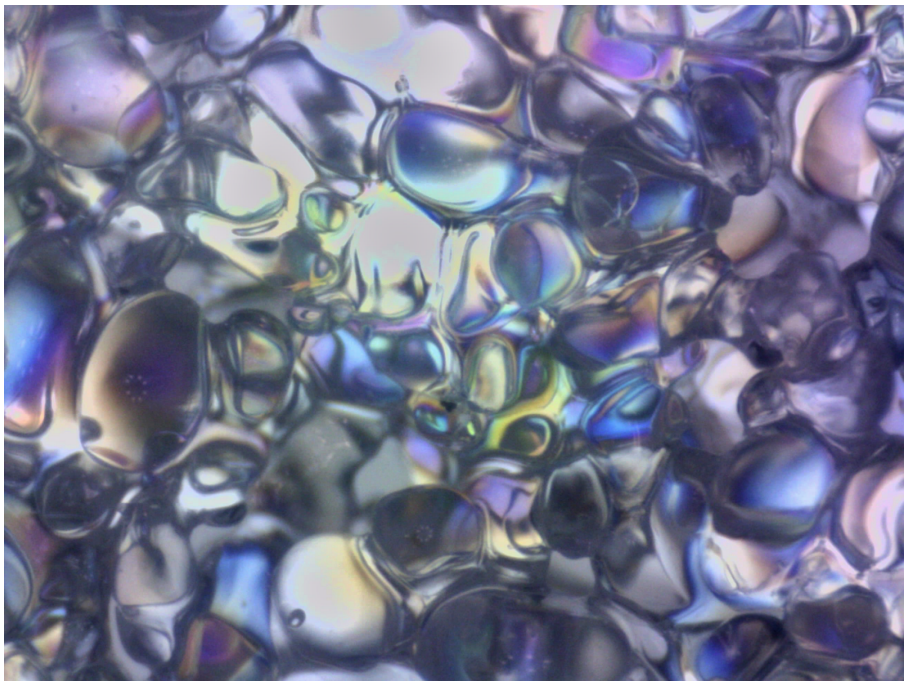

Snow contamination of cars

Collisions of ice particles with surfaces

Tobias Eidevåg

Chemical Engineering Division
Department of Chemistry and Chemical Engineering

CHALMERS UNIVERSITY OF TECHNOLOGY

Gothenburg, Sweden, 2020

Snow contamination of cars

Tobias Eidevåg

Licentiatuppsatser vid Instutitionen för kemi och kemiteknik
Chalmers tekniska högskola
SE-412 96 Göteborg
Nr 2020:15.

Department of Chemistry and Chemical Engineering
Chemical Engineering Division
Chalmers University of Technology
SE-412 96, Gothenburg
Sweden

Cover
Microscope sample of spherical snow grains reflecting a blue winter sky.

Printed by Chalmers Reproservice,
Gothenburg, Sweden 2020.

Abstract

Seasonal snow cover on roads causes car accidents that lead to human suffering and economic loss. Snow cover decreases visibility and road-tire friction. Advanced active safety systems have been developed to cope with sudden changes in driving conditions and have been engineered to act as quickly as possible. These systems are heavily reliant on sensors on the exterior of the car that can detect these changes. Snow, however, has a tendency to accumulate and cause sensor blockage, and consequently, the sensors might not be available when they are most needed.

The physics of how snow and ice adhere to surfaces must be understood in order to develop measures that avoid snow accumulation. Snow and ice during normal winter temperatures in the northern hemisphere (0° C to $\sim -30^\circ$ C) are close to the melting point of ice and are therefore thermodynamically active. This fact in combined with small grain sizes causes ice and snow to easily adhere to surfaces.

Mathematical models for snow adhesion are developed in this work by studying collisions of ice particles with walls. Based on a general theory for adhesive-elastic interactions, the threshold velocities for ice particles are calculated so that particles that collide with surfaces at velocities below this threshold will adhere to the surface they collide with. Experimental measurements are also conducted on ice particles that collide with different massive walls, and from these measurements, a collisional melting model is proposed to model the abrupt increase in energy loss observed. The two different modeling approaches are combined as a generalized velocity-dependent collision model for ice particles.

Keywords

Snow adhesion, ice adhesion, particle impacts, coefficient of restitution, premelting, radar blockage

Acknowledgments

I am deeply grateful to everyone that has been involved in the research process leading up to this licentiate. First, I want to thank my supervisor, Anders Rasmuson, for giving me the freedom and encouragement I needed as a research student. Thank you for always being available, taking the time to review my work, and always being open to discuss anything from ice particles to hiking trips.

I would like to thank everyone in Fluid and Experimental Mechanics at Luleå University of Technology for their warm welcoming during my research visit. I also wish to thank my co-supervisor Johan Casselgren at Luleå University of Technology for always being positive and open to discussing new ideas for ice and snow measurements.

I would like to extend my sincerest thanks to Erik Thomson at Gothenburg University for taking the time to discuss the thermodynamics of ice and snow and for the great feedback when I was working on Paper II.

I would like to express my gratitude to Matthias Eng at Volvo Cars for initiating the research project and supporting me when the research project started up, and thanks also to David Kallin at Volvo Cars who continued in Matthias footsteps and helped me stay on a relevant path in my research.

I would like to thank all my great colleagues at both workplaces! To Contamination and Core CFD at Volvo Cars for your support and friendliness, thanks for many cheerful winter adventures in northern Sweden. Thanks to everyone at Chemical Engineering at Chalmers for the welcoming atmosphere.

Thanks to "my own" previous and current thesis students. Thank you all for your great work, and thanks for giving me the opportunity to mentor you in your thesis work. I hope you all have learned as much working with me as I have done by mentoring you.

Thanks to Vinnova and Volvo Cars for funding the research in this thesis.

Finally, I want to express my gratitude to my close friends and family who are always there for me. Thanks to my best friend, wife, and love of my life, Emily, for her patience and encouragements.

List of Publications

Appended publications

This thesis is based on the following publications:

[A] T. Eidevåg, P. Abrahamsson, M. Eng, A. Rasmuson

"Modeling of dry snow adhesion during normal impact with surfaces"
Powder Technology, 361, 1081–1092. 2020.

[B] T. Eidevåg, E. S. Thomson, S. Sollén, J. Casselgren, A. Rasmuson
"Collisional damping of spherical ice particles"
In submission to Powder Technology.

Research Contribution

Paper I: I implemented the contact models in the software, and I designed and performed the DEM simulations. I performed the evaluation of the results with feedback from the co-authors.

Paper II: I performed the experiments with help from Sofia Sollén. I designed and performed the image analysis of the experiments. I evaluated the experimental results together with the co-authors. I developed the novel model proposed in the paper. I wrote the first draft of the manuscript.

Contents

Nomenclature

Latin symbols

a	–	Contact radius [m]
a_0	–	Equilibrium radius [m]
a_d	–	Maximum contact radius [m]
A_H	–	Hamaker coefficient [J]
e_n	–	Coefficient of restitution
d	–	Liquid layer thickness
E^*	–	Effective Young's modulus [Pa]
E_i	–	Impacting kinetic energy [J]
E_v	–	Energy loss due to viscous damping [J]
E_s	–	Energy to stick at collision [J]
F_n	–	Normal contact force [N]
F_t	–	Tangential contact force [N]
F_c	–	Pull-off force [N]
F_v	–	Viscous damping force [N]
f_t	–	Sliding friction coefficient
f_r	–	Rolling friction coefficient
G	–	Interaction energy [J/m^2]
G_0^+	–	Potential energy barrier [eV]
k_b	–	Boltzmann constant [eV/K]
l	–	Separation distance [m]
m^*	–	Effective mass in contact [kg]
m	–	Mass of particle [kg]
M_c	–	Critical torque [Nm]
P_m	–	Bulk melting pressure [Pa]
q_m	–	Latent heat of fusion [J/kg]
R	–	Particle radius [m]
R^*	–	Effective particle radius [m]
T	–	Temperature [K]
T_H	–	Homologous temperature
T_m	–	Bulk melting temperature [K]
V_r	–	Rebound velocity [m/s]
V_c	–	Critical impact velocity [m/s]
V_i	–	Impact velocity [m/s]
V_s	–	Stick velocity [m/s]
V_t	–	Tangential velocity [m/s]
W	–	Work of adhesion [J/m^2]

Greek symbols

ε	–	Particle roughness [m]
δ	–	Normal overlap [m]
δ_c	–	Critical normal overlap [m]
δ_r	–	Rolling displacement [m]
$\delta_{r,c}$	–	Critical rolling displacement [m]
δ_t	–	Tangential displacement [m]
ϵ	–	Dielectric constant
$\Delta\gamma/\gamma$	–	Adhesion hysteresis for rolling
γ	–	Surface energy [J/m^2]
ν	–	Poisson's ratio
η	–	Viscosity [Ns/m]
μ_q	–	Chemical potential of quantity q [J/kg]
ρ_p	–	Particle density
ρ_l	–	Liquid phase density
ρ_s	–	Solid phase density
θ	–	Contact angle [rad]
ξ	–	Fraction of kinetic energy converted to damage

Acronyms

ADAS	–	Advanced Driver Assistance Systems
CFD	–	Computational Fluid Dynamics
CDT	–	Directional Constant Torque
DT	–	Dominik and Tielens
DEM	–	Discrete Element Method
JKR	–	Johnson, Kendall, and Roberts
LIGGGHTS	–	LAMMPS Improved for General Granular and Granular Heat Transfer Simulations
QLL	–	Quasi-Liquid layer

Chapter 1

Introduction

1.1 Vehicle sensor contamination caused by snow

Safety systems in vehicles in recent years have extended from passive safety systems, such as airbags and seat belts to include active safety systems, Advanced Driver Assistance Systems (ADAS). This development has led to reductions in accidents. For example, insurance data reveal that collision-avoidance features have reduced rear-end collisions by 37% in Sweden [1].

On-board sensors, such as cameras, lidar, and radar sensors, give input to the ADAS [2]. The ADAS then interpret these inputs and execute tasks depending on the situation, for example, path planning, collision avoidance, and taking control of the vehicle [2]. ADAS is, therefore, dependent on the availability of these sensors. This is a challenge in harsh weather conditions where deposits of water, snow, ice, or dirt impair the performance of these sensors, causing false input or no input at all to the ADAS. A particularly challenging problem is sensor contamination due to winter road conditions. A recent study tested different lidar sensors, and all the tested sensors malfunctioned during a snow test [3].

Winter season causes snowy roads in a large area in the northern hemisphere. For example, over 70 % of the US population lives in areas with annual snowy regions [4]. Many drivers can therefore be affected by sensor contamination due to the potential malfunction of safety systems. At the same time, annual winter weather reduces visibility and decreases pavement friction, which increases the likelihood of vehicle accidents. Snowy roads account for 24% of all weather-related vehicle crashes in US [4]. Active safety systems for these roads are likely to be less available at the same time as they are potentially needed the most. The problems associated with sensor contamination increase with the increased progress in active safety systems. Many car manufactures are working on developing self-driving cars, which is an ADAS system where the main functionality of the car (driving) is completely dependent on the input from vehicle sensors. Three main scenarios of driving can cause sensor contamination on a car on a winter road: self-contamination, third-party contamination, and contamination due to snowfall. Self-contamination is caused by to the car wheels lifting snow from the ground and contaminating the car itself. This type of contamination is always present if there is a sufficiently thick snow layer on

Figure 1.1: Self-contamination

Figure 1.2: Third-party contamination

the road, and snow often accumulates in low air velocity regions at the rear of the car. Third-party contamination is the driving scenario where the car of interest is close behind another vehicle and is affected by the snowy wake of the other vehicle. This scenario is typically the worst when the front vehicle is larger than the car of interest, for example, a truck. For this scenario snow can accumulate on all surfaces on the vehicle, but since self-contamination is always present in practice, the observed difference is often that snow also tends to adhere and accumulate at the front of the car. Visibility for the driver is often very low. Contamination due to falling snow is the scenario of a car driven in snowfall that is less well defined than the other two scenarios. Snow, which consists of ice grains and pore space [5], are typically consisting of spheroid ice particles for the other two scenarios [6] but for this scenario the snow usually consist of complex snowflakes that can take a wide range of shapes depending on the temperature [7]. The scenario itself is also heavily dependent on the amount of falling snow, which can range from a light snowfall that is almost invisible for the human eye to heavy snowfall. This thesis mainly focuses on the first two contamination scenarios, and they are shown in Figure 1.1 and Figure 1.2.

The prediction of possible sensor contamination given a defined driving condition during the design and development of a new car model is important engineering feedback. The shape and positioning of a sensor can be optimized. Today most verification's for harsh weather conditions, such as snow contamination, are done on winter test tracks or climate wind tunnels. This requires a complete vehicle test with finalized hardware and software and are therefore performed in late stages of the product development. The largest part of the development of a new car model occurs virtually, and it is costly to make major changes to the design when the first prototypes of the car are built. For these reasons, there is a strong need for simulation models that predict effects on sensors during winter conditions. There is a specific need for models that can predict where snow is likely to stick to exterior surfaces on a vehicle, and how much snow can accumulate on a certain location on the vehicle. In recent years, new studies have proposed different models for how these predictions can be done. The models are often based on Computational Fluid Dynamics (CFD) where an aerodynamic field is simulated, and particles are injected into this field [8–11]. The particles can then be traced in time, and a collision with a vehicle surface can be recorded as a possible impingement on a surface. These

studies have primarily focused on aerodynamics and the multiphase interaction of particles with a turbulent field, while little attention has been given to material properties and the elastic-adhesive interactions in particle-wall and particle-particle collisions for snow. These interactions for any material are known in general to be size-dependent where small particles tend to adhere to surfaces more than large particles. It is also well documented that the adhesive properties of snow and ice, are temperature sensitive [12, 13] i.e. the adhesive forces increase when approaching the melting point of water.

This thesis addresses and discusses snow and ice adhesion to develop new models that predict sensor contamination on a vehicle in winter road conditions. Transferring challenging weather phenomena into mathematical models that capture the underlying physics can have many positive outcomes. The intention of the present research was primarily to predict when snow will adhere and accumulate upon collision with surfaces. Nevertheless, with an increased understanding of snow adhesion, the thesis also aims to address how snow adhesion can be avoided. The results in this work are intended to be general, enabling them to be applied to any situation where snow adheres and accumulates on surfaces.

1.2 Aim and objectives

This thesis aims to establish mathematical models for snow adhesion. This is achieved by addressing the following objectives

- To derive computational models for ice particle impacting on massive walls at different velocity regimes.
- To provide a detailed analysis of how material properties affect snow adhesion.
- To investigate what role temperature plays in the current research problem based on snow and ice physics.

Chapter 2

Particles in contact

Snow adhesion and the associated sensor contamination involve particles that interact with other objects upon collision (particles or walls). These interactions define whether a particle will stick or bounce. This chapter presents some of the fundamental concepts for particle-particle and particle-wall interactions and combines static interactions that depend on intermolecular forces with dynamic interactions that depend on the collision process. This thesis uses expressions such as "energy loss" and "dissipation of energy" to describe when kinetic energy upon a collision is transferred or transformed in such a way that the particle speed decreases and the transferred or transformed energy no longer affects the particle.

It is worth emphasizing that this thesis focuses on macroscopic particles, i.e. particles that are at least micrometer-sized. Some of the continuity and macroscopic assumptions made do not apply as the particle size decreases and approaches nanometer size.

2.1 Intermolecular interaction

Particle ability to adhere to an object generally has many sources. This ability can be due to capillary adhesion, chemical bonding, or intermolecular forces, for instance. Intermolecular forces are one of the most common sources of adhesion and occur due to electrodynamic interactions between molecules and/or atoms. These forces are often attractive but can also be repulsive. Intermolecular forces can be divided into three different forces depending on the electron fields in the interaction: Dipole-dipole (Keesom), Dipole-induced dipole (Debye), and induced dipole-induced dipole (London/Dispersion) [14]. These forces are collectively often called the van der Waals forces. The terminology is unfortunately not consistently used in the literature and sometimes the term "van der Waals forces" is only used for dispersion forces. No distinction is made between the different types of forces in this thesis and all electrodynamic intermolecular forces will be referred to as van der Waals forces.

If van der Waals forces are long-range or short-range depends upon the perspective. In nanoscale science, they are often referred to as "long-range" since they act longer than an atomic bond length [15]. These forces are also significantly longer than hydrogen bonds or chemical bonds [14]. However, it

could also be argued, that for macroscopic particles (larger than nanometer-sized) these forces are "short-range" since they are only present when particles are in contact. The effects of van der Waals forces grow as objects get smaller since the ratio between surface area and the mass of a particle grows with decreasing size. The interaction energy per unit area between two flat plates of different materials in a medium based on the Lifshitz theory of van der Waals forces is defined as [14]

$$G(l) = \frac{A_H}{12\pi l^2}, \tag{2.1}$$

where l is the separation distance, and A_H is the effective Hamaker coefficient for the two materials in the medium. For applications with air as a medium, it is often assumed that this is similar to no medium at all (vacuum). The A_H is mainly determined by material properties and can be calculated using the dielectric functions of the materials [16]. The adhesive force per unit area for two rigid spheres can be estimated using the Derjaguin approximation as [14]

$$F(l) = 2\pi R^* G(l), \tag{2.2}$$

where

$$R^* = \frac{R_1 R_2}{R_1 + R_2}, \tag{2.3}$$

is the effective radius of the contact, and R_1 and R_2 are the radii for the two objects in contact. For a particle-wall interaction $R_2 = \infty$ and thus $R^* = R_1$.

2.2 Adhesive-elastic interaction

The force in equation (2.2) is valid for completely rigid particles. However, real particles are never completely rigid, and they deform elastically upon contact [14]. This deformation can occur due to externally applied forces as well as intermolecular forces that either push or pull the contact. A theory that predicts this elastic deformation due to intermolecular forces is the JKR model, which is an extension of the Hertz contact theory. The JKR model was formulated by Johnson, Kendall, and Roberts (1971) and is still today a basis for modern theories of how to model adhesion [14]. While the Hertz model predicts a linear relation between normal contact force F_n and central displacement δ, the JKR model predicts a nonlinear relationship. The δ is the difference between the undeformed and deformed radius of the particle at contact. In this model, F_n can be both attractive and repulsive, while it is always repulsive in Hertz model. The pull-off force F_c in the JKR model, which is the force needed to detach a particle in contact, is defined as

$$F_c = \frac{3}{2}\pi R^* W, \tag{2.4}$$

where W is the Work of adhesion, the amount of work required to separate two flat surfaces from contact to infinity. W can be estimated using equation (2.1) for a fixed distance upon contact $l = z_0$ so that $W = G(z_0)$, however, this will then be sensitive to the choice of z_0. The dielectric functions of the materials are not always known such that A_H can be calculated. Another way

to calculate W is based on surface energies [14], for two objects with the same material W is simply

$$W_{11} = 2\gamma_1. \tag{2.5}$$

Rules how to combine surface energies are typically applied for dissimilar materials. Fowkes [17] has composed surface energies into dispersive and a-scalar contributions as

$$\gamma = \gamma^d + \gamma^a, \tag{2.6}$$

where W can then be approximated as

$$W_{12} = 2(\sqrt{\gamma_1^d \gamma_2^d} + \sqrt{\gamma_1^a \gamma_2^a}). \tag{2.7}$$

however, when dispersion forces are responsible for most of the interaction, W_{12} can be calculated as [14]

$$W_{12} = 2\sqrt{\gamma_1^d \gamma_2^d}. \tag{2.8}$$

As shown by Chokshi et al. [18], the JKR model can be written in the dimensionless form as

$$\frac{F_n}{F_c} = 4\Big(\frac{a}{a_0}\Big)^3 - 4\Big(\frac{a}{a_0}\Big)^{\frac{3}{2}}, \tag{2.9}$$

and

$$\frac{\delta}{\delta_c} = 6^{\frac{1}{3}}\left(2\Big(\frac{a}{a_0}\Big)^2 - \frac{4}{3}\Big(\frac{a}{a_0}\Big)^{\frac{1}{2}}\right). \tag{2.10}$$

where a is the contact radius, a_0 is the contact radius at equilibrium, and δ_c is the critical displacement, which is the separation distance needed for the contact to break. These variables are defined as

$$\delta_c = \frac{a_0^2}{2(6)^{\frac{1}{3}} R^*}, \tag{2.11}$$

and

$$a_0 = \left(\frac{9\pi W R^{*2}}{2E^*}\right)^{\frac{1}{3}}. \tag{2.12}$$

The effective Young modulus E^* is defined as

$$\frac{1}{E^*} = \frac{1-\nu_1^2}{E_1} + \frac{1-\nu_2^2}{E_2}, \tag{2.13}$$

where E_k is the Young modulus, and ν_k is the Poisson's ratio of material k.

Equations (2.9) and (2.10) give F_n as an implicit function of δ that can only be solved numerically. The relationship between F_n and δ is shown in Figure 2.1 where the dimensionless F_n/F_c is plotted as a function of δ/δ_c. Four points of interest are highlighted in the figure: A, B, C, and D, which are ordered for a collision in the sequence of events. Figure 2.2 shows exaggerated illustrations of the particle deformations at these four points for a particle upon collision with a wall. A is the initial contact point when $\delta = 0$, and the model then predicts an attractive contact force ($F_n < 0$). The particle therefore accelerates

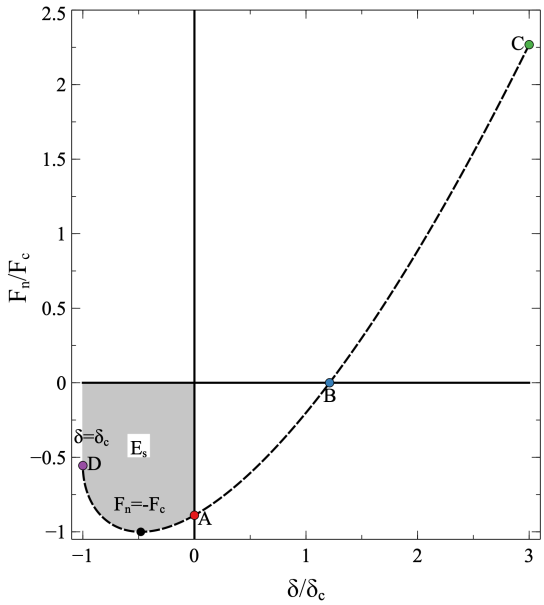

Figure 2.1: Contact force F_n/F_c for the JKR model as a function of central displacement δ/δ_c where both quantities are plotted in dimensionless form. Notation shows four points of interest: A - Initial contact point, B - Equilibrium point, C- Maximum compression point, and D - Critical tear-off point.

towards the wall. At point B, which is the equilibrium point, the contact force is zero, and after this point, the particle will experience a repulsive contact force ($F_n > 0$) and subsequently decelerate. This will occur up to point C, which is the maximum compression point, where the velocity of the particle will be zero and the particle will start to rebound. The particle will then rebound and accelerate from C to B and then decelerate again until point A. If there is only energy dissipation due to adhesive-elastic interaction, there will so far be no loss of energy for the particle since the force path going from $A \rightarrow B \rightarrow C$ is the same as going from $C \rightarrow B \rightarrow A$. After this, the JKR model predicts a necking stage of the contact, i.e. even though δ is negative, there is still a contact due to a deformed contact neck and subsequently an attractive contact force ($F_n < 0$) up to point D, which is the point of critical displacement when $\delta = -\delta_c$. This extra force path from A to D causes energy loss E_s in a collision, and it can be calculated as

$$E_s = F_c\delta_c \oint_{A->C->D} \frac{F_n}{F_c} d\Big(\frac{\delta}{\delta_c}\Big) = F_c\delta_c \int_D^A \frac{F_n}{F_c} d\Big(\frac{\delta}{\delta_c}\Big) = K_1 F_c \delta_c, \qquad (2.14)$$

where $K_1 \approx 0.936$ is an integration constant, and the resulting value of the integral is illustrated in shaded gray above line for F_n/F_c in Figure 2.1. E_s is the kinetic energy needed for a particle to rebound, and the critical impact velocity V_s can be formulated from this equation as [19]

$$\frac{1}{2} m^* V_s^2 = E_s, \qquad (2.15)$$

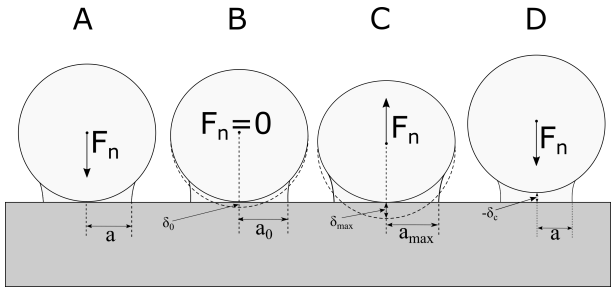

Figure 2.2: Illustration of different points of interest during a particle-wall collision: A - Initial contact point, B - Equilibrium point with no contact force, C - Maximum compression point, and D - Critical tear-off point.

m^* is the effective mass in the collision defined as

$$\frac{1}{m^*} = \frac{1}{m_1} + \frac{1}{m_2}, \tag{2.16}$$

where m_1 and m_2 are the mass of particles 1 and 2. The velocity V_s is the minimum V_i needed for a particle to rebound, and a particle will adhere to the colliding object if $V_i < V_s$ according to the JKR model. Inserting expressions for δ_c and F_c, it follows that

$$V_s = \sqrt{\frac{9K_1}{4m^*}}\left(\frac{\pi^5 W^5 R^{*4}}{E^{*2}}\right)^{\frac{1}{6}}, \tag{2.17}$$

which for a particle colliding with a massive wall simplifies to

$$V_s = \frac{3\sqrt{3}}{4}\sqrt{\frac{K_1}{\rho}}\left(\frac{\pi^2 W^5}{R^5 E^{*2}}\right)^{\frac{1}{6}}. \tag{2.18}$$

Two interesting observations can be made from equation (2.18). First, $V_s \propto R^{-5/6}$, which means that smaller particles will tend to stick at higher velocities. Second, the V_s is also proportional to the interaction properties W and E^* as $V_s \propto W^{5/6} E^{*-1/3}$. This means that V_s will increase with an *increase* in W or a *decrease* in E^*.

The coefficient of restitution e_n is defined for a particle-particle or particle-wall collision as the square root of the ratio between rebound kinetic energy E_b and incoming kinetic energy E_i. For a particle with constant mass, this simplifies as

$$e_n = \sqrt{\frac{E_b}{E_i}} = \frac{V_r}{V_i}, \tag{2.19}$$

where V_i is the impact velocity and V_r is the rebound velocity. This can also be formulated as a function of V_s [19]. For the loss caused by adhesive-elastic interactions predicted by the JKR model, e_n can be expressed as

$$e_n = \sqrt{1 - \left(\frac{V_s}{V_i}\right)^2}. \tag{2.20}$$

For $V_i < V_s$, it follows that $e_n = 0$ and $e_n$will rapidly increase towards 1 with increasing V_i. Figure 2.3 shows e_n as a function of V_i/V_s.

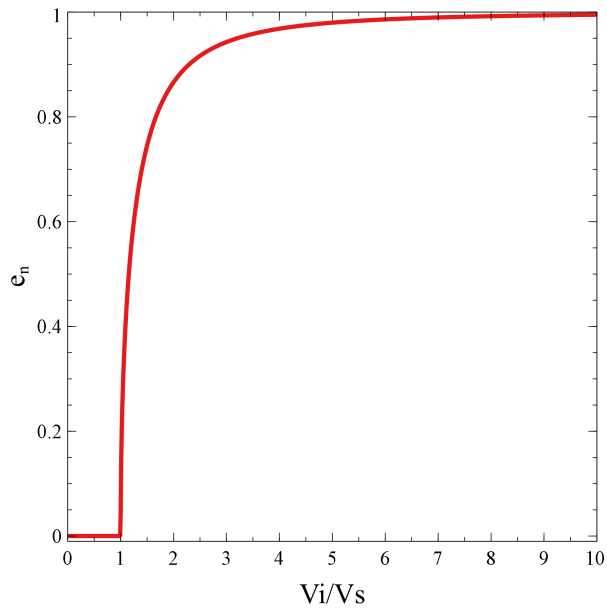

Figure 2.3: The coefficient of restitution e_n caused by intermolecular forces as predicted by the JKR model as a function of V_i/V_s.

2.2.1 Tangential adhesive-elastic interactions

While the JKR model is a well-established theory for adhesive-elastic interactions in the normal direction relative to a contact, models in the tangential direction are not as established. Tangential interactions are especially important for oblique impacts but can also be a major source of energy loss for agglomerate impacts [20]. If tangential forces act on a particle in contact with a particle or a wall it can slide or roll. This will depend on which resistance is the lowest, and the particle will then either move at a certain tangential velocity v_t or rotate with an angular velocity Ω. The particle and the contact will then deform. This is illustrated in Figure 2.4. A simplified approach to modeling the resistance of adhesive particles to sliding has been proposed by Thornton [19], where sliding is related to F_n, F_c, and the friction coefficient f_t as

$$F_t = f_t|F_n + 2F_c|, \tag{2.21}$$

where F_t is then the tangential resistance force. Theoretically, however, this will only apply to rigid particles and a resistance force lower than F_t can cause elastic deformation that store energy that can later be released. f_t can be viewed as a material property, but it can also be increased to model the surface roughness of a particle. Sliding is rarely seen for adhesive particles, and modeling of this resistance is mainly done to avoid sliding so particles instead roll [21].

Multiple ways to model the adhesive rolling resistance of particles have been proposed in the literature. A comprehensive model based on the asymmetric pressure distribution at the contact point has been proposed by Dominik and Tielens [22]. This model will hereinafter be referred to as the DT model. The

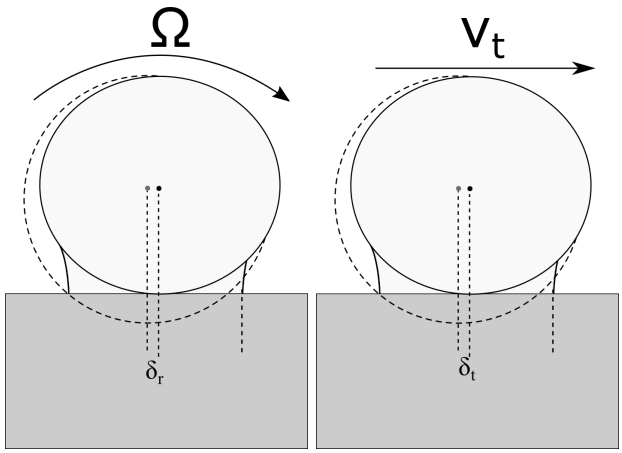

(a) Rolling (b) Sliding

Figure 2.4: Adhesive-elastic tangential particle interactions with a wall.

DT model assumes perfect spherical particles where the critical torque for irreversible rolling is defined as

$$M_c = 4F_c\Big(\frac{a}{a_0}\Big)^{3/2}\delta_r, \tag{2.22}$$

where $\delta_{r,c}$ is the critical rolling distance. Krijt et al. [23] showed that $\delta_{r,c}$ can be expressed in terms of a_0 and a new term, the adhesion hysteresis for rolling $\Delta\gamma/\gamma$, as

$$\delta_{r,c} = \frac{a_0}{12}\frac{\Delta\gamma}{\gamma}. \tag{2.23}$$

In this model, $\frac{\Delta\gamma}{\gamma}$ is a material parameter that can be obtained based on experimental data.

2.3 Plastic dissipation

Apart from losses due to intermolecular forces many other interactions can cause an inelastic collision and thereby cause particles to adhere to a surface. Thornton and Ning [24] have proposed an extension of the JKR model with the plastic deformation of particles. The theory is that plastic deformation occurs in the contact given that a limiting contact pressure p_y has been reached. The deformation causes a loss in kinetic energy for a particle, and the e_n caused by plastic dissipation for a particle colliding with a massive wall has been derived by Thornton and Ning [24] as

$$e_n = 1.324\Big(\frac{p_y^5}{E^{*4}\rho_p}\Big)^{1/8}V_i^{-1/4}, \tag{2.24}$$

where ρ_p is the particle density.

2.4 Capillary adhesion

The forces in a particle-particle or particle-wall contact can drastically change in the presence of a liquid due to capillary forces [14]. A static contact has two main contributions to the capillary forces: the Laplace pressure contribution and the contribution from the adhesive force inside the liquid annulus. The sum of these forces is [14]

$$F = \frac{4\pi R^* \gamma_{lv} \cos(\theta)}{1 + x/d} + 4\pi R^* \gamma_{sv}, \tag{2.25}$$

where θ is the contact angle. The first term in this sum is the Laplace pressure contribution, and the second term is the adhesive force inside the liquid annulus.

For the dynamic contact when a particle collides with another particle or a wall, there is also a viscous damping force F_v caused by the viscosity η of the liquid. This force is velocity-dependent. Matthewson [25] has shown based on Reynolds lubrication theory that for a particle colliding with a wall, F_v can be related to the particle velocity V as

$$F_v = 6\pi\eta R^2 V h(x), \tag{2.26}$$

where $h(x)$ is a function of the separation distance x between the particle and the wall. For an infinite wetted wall, Chan and Horn [26] have shown that

$$h(x) = 1/x, \tag{2.27}$$

which agrees well with their experimental findings, except for very thin layers or small separation distances. This equation diverges when $x \to 0$ and F_v is often limited for $x \leq \varepsilon$ where ε is a certain length scale, often taken as the particle roughness [27].

$h(x)$ is more complex when the wetted wall is a finite size since it depends on the meniscus geometry. Matthewson [25] has derived for a contact with a finite wetted wall that

$$h(x) = \left(1 - \frac{x}{x + a_w^2/(2R)}\right)^2 \frac{1}{x}, \tag{2.28}$$

where a_w is the wetted radius of contact and equation (2.28) reduce to equation (2.27) for $a_w \to \infty$. To estimate the associated energy loss E_v for a particle colliding with a wall, F_v can be integrated over the collision path as

$$E_v = \oint F_v dx. \tag{2.29}$$

The resulting energy loss E_v for $h(x)$ using equation (2.27) with a limit when $x \leq \varepsilon$ has been estimated by Sutkar et al. [27] to be

$$E_v = \frac{3}{2}\pi\eta R^2 V_i \ln(\frac{d}{\varepsilon}). \tag{2.30}$$

To the best of our knowledge, no similar integration result has been published for $h(x)$ using equation (2.28).

2.5 Particle simulations

Simulations of particles, where the intention is to track the position of a particle in time, is usually done by solving Newton's second law of motion as

$$m\frac{d^2\boldsymbol{v}}{dt^2} = \sum_{\forall i} \boldsymbol{F_i}. \tag{2.31}$$

In this equation symbols in ***bold*** refer to vectors in 3D where $\boldsymbol{v}$ is the particle velocity, m is the mass of the particle, which is assumed constant, and the sum of all $\boldsymbol{F_i}$ represents all forces acting on a particle at a specific time-step. This force can, for example, be drag force, lift force, gravity, or contact force in a collision. If a particle is also allowed to rotate, then Newton's law of rotation is also solved

$$I\frac{d\boldsymbol{\Omega}}{dt} = \sum_{\forall i} \boldsymbol{M_i}, \tag{2.32}$$

where I is the particle inertia, $\boldsymbol{\Omega}$ is the angular velocity of the particle, and the sum of all moments $\boldsymbol{M_i}$ represents all moments acting on the particle. Particle-particle or particle-wall interactions can be modeled with either binary collisions, also called the hard-sphere approach, or by resolving the collision with the soft-sphere approach [28]. The soft sphere approach is commonly called the Discrete Element Method (DEM), which allows particles to overlap, and the force is then expressed as functions of this overlap. δ is equivalent to this overlap in the JKR model as defined by equation (2.9) and equation (2.10), and thus these equations can be used directly as they are for DEM.

Chapter 3

Physics of snow and ice

Following the international classification for seasonal snow on the ground [5], this work defines snow as a highly porous material consisting of ice grains and pore space. For clarity, terminology such as "snow particle" or "snow grain" is avoided, and instead, individual "pieces" of snow are referred to as ice grains or ice particles. Particles that are in weak contact with each other and form a cluster of particles are referred to as agglomerates. This contrasts with the term aggregate, which will be used for clusters of ice particles strongly bonded together by melt-freeze cycles. In the literature, it is common to classify snow as either wet or dry, depending on if the snow is at or below its melting temperature [29]. This is not necessarily the standard bulk melting temperature of water ($0°C$) since melting-point depression can occur caused by ionic impurities or curvature [30]. This thesis mainly examines dry snow defined as snow that is below its melting point. However, the usage of the word "dry" in the classification could be challenged since liquid-water does exist on the surface of ice at thermodynamic equilibrium for temperatures well below the bulk melting temperature of water.

Snow is defined herein as a granular material consisting of ice particles, and therefore, the physics of ice holds the key to understanding snow. Ice is close to its melting point in natural weather conditions on earth, and there are many interesting ongoing processes for ice and snow such as sintering, sublimation, and metamorphism. A measure of how close a material is to its melting temperature is its homologous temperature, which is defined as

$$T_H = \frac{T}{T_m}, \tag{3.1}$$

where T is the material temperature, T_m is the bulk melting temperature, both in Kelvin. A homologous temperature of 80% for ice corresponds to a temperature of $-55°$C. Intuition from our daily life might suggest that this is a low temperature, but for a crystalline material such as ice this is regarded as a high temperature [31]. As a comparison, a homologous temperature of 80% for iron or silver would correspond to 1174 °C or 714 °C. Ice at $T = 263$ K corresponds to $T_H = 0.96$, which is an exceptionally high value of T_H and can be compared to stones heated to 1414 K, commonly called lava.

3.1 Snow morphology

Ice crystals are formed in the troposphere through collisions of supercooled nanometer-sized liquid droplets and aerosol particles. These particles cause the droplets to nucleate at an elevated temperature [32]. Driven by the curvature of these small droplets, the droplets first nucleate at temperatures around -38 °C without aerosol particles, due to the Gibbs-Thomson effect. Once an ice crystal has formed, it grows through deposition where surrounding water vapor transforms into solid ice on the crystal. This occurs while the crystal falls from the sky, and the resulting shape of the crystal is affected by the local humidity surrounding the crystal, the air temperature, and the path of the falling crystal. The resulting crystal is commonly referred to as a snowflake, and due to variations in weather, these snowflakes can take many different forms such as needles, columns, prisms, or dendrites [33].

A snowflake has a high specific surface area, and the T_H for seasonal snow covers is typically close to 100%. Therefore, a settled snowflake on the ground is thermodynamically very active and will rapidly begin to change size and shape, called snow metamorphism [29]. There exists two categories of snow metamorphism for snow below its melting temperature: the equilibrium form and the kinetic growth form. Kinetic growth occurs at a fast rate of growth where humidity causes deposition, and the crystal takes a hexagonal form. The equilibrium form, in contrast, occurs at slower growth rates, where individual ice grains approach a spherical shape and can either grow or shrink in size [29]. Since ice is so close to its melting temperature, it can easily change phase from solid to liquid (melt) or from solid to vapor (sublimation). This process is driven by the minimization of the energy state and is sensitive to humidity, temperature gradients, and the curvature at the ice surface [29]. The metamorphism for snow affects the particle size distribution expected for ice particles in a snow cover [34], e.g. particles with a radius of 1 μm have such a high curvature that they are expected to disappear (by sublimation) within 1 hour, while particles of 100 μm are expected to disappear in 1 year [35]. Langlois et al. [36] have studied the particle size distribution of the seasonal snow cover in northern Canada and found that round particles were a few hundred microns to one millimeter in size with an average diameter of 700 μm. An infield study on road snow found similar sizes for spherical ice particles on the ground, but it has also been found that the particles adhering to the rear tail light of a car while driving were significantly smaller, and a peak value was found at a diameter of 50 μm [6].

3.2 The premelting of ice

A crystalline material can start to form a disordered structure among the top molecules at the interface between the material and the vapor (i.e. at the surface of the material) when the material is close to its melting point. The molecules form a distorted structure of a certain stable thickness often called a quasi-liquid layer (QLL) with properties between solid and bulk water liquid [37]. This phenomenon is called premelting and can occur on a surface in contact with vapor (surface melting) or can occur at the interface between two objects (interfacial melting). Premelting occurs for many crystalline materials,

e.g. in ceramics [38] or ice [39], which is the focus of this chapter. As early as 1842, Michael Faraday postulated the existence of a liquid layer on ice below its melting point and proved this experimentally [39]. This was disputed by James Thomson who instead incorrectly accredited the experimental results to pressure melting [40]. For a long time, the theory of premelting was overlooked by the scientific community and new experiments were conducted in the 1950s providing evidence of the existence of a premelted QLL on ice [13]. The premelting of ice is currently a very active research field with many recent studies investigating the implications of a QLL. 70% of earth is covered by water, and premelting has been found to explain many interesting environmental phenomena on earth such as the possibility to ice skate [40], mass charges of thunderstorms [41], frost heave [42], and glacier movement [42].

The presence of a QLL can be explained with interfacial thermodynamics. A derivation for the QLL thickness d in thermodynamic equilibrium will now be presented based on the work by [41–43]. As a start, consider a solid to be in thermodynamic equilibrium with a vapor at temperature T and pressure P. If there is finite QLL of thickness d, the free energy per unit area of this layer will be the sum of the free energy of the bulk and surface terms, i.e.

$$G_{qll}(T, P, d) = [\rho_l \mu_l(T, P)]d + F_{total}, \tag{3.2}$$

where ρ_l is the density of the liquid, F_{total} is the total excess surface free energy per unit area, and $\mu_l(T, P)$ is the chemical potential of the bulk liquid. The chemical potential of the QLL is then

$$\mu_{qll}(T, P, d) = \frac{1}{\rho_l}\frac{\partial G_{qll}}{\partial d} = \mu_l(T, P) + \frac{1}{\rho_l}\frac{\partial F_{total}}{\partial d}. \tag{3.3}$$

In thermodynamic equilibrium, μ_{qll} is equal to the chemical potential of the solid μ_s, i.e.

$$\mu_{qll}(T, P) = \mu_l(T, P) + \frac{1}{\rho_l}\frac{\partial F_{total}}{\partial d} = \mu_s(T, P). \tag{3.4}$$

This equation implies a difference in chemical potential between the solid and the bulk liquid caused by the derivative of the total excess surface free energy. This causes a displacement of phases, which can be evaluated using a Taylor series expansion as

$$\Delta\mu(T, P) = \mu_s(T, P) - \mu_l(T, P) = \frac{q_m}{T_m}(T_m - T) + \frac{\rho_l - \rho_s}{\rho_l \rho_s}(P_m - P), \tag{3.5}$$

where q_m is the latent heat of fusion, and ρ_s is the density of the solid. Combining equation (3.4) and equation (3.5), it follows that

$$\Delta\mu(T, P) = \frac{1}{\rho_l}\frac{\partial F_{total}}{\partial d} = \frac{q_m}{T_m}(T_m - T) + \frac{\rho_l - \rho_s}{\rho_l \rho_s}(P_m - P), \tag{3.6}$$

Using equation (2.1), the derivative of the total excess surface free energy per unit area can be expressed as

$$\frac{\partial F_{total}}{\partial d} = -\frac{A_H}{6\pi d^3}, \tag{3.7}$$

where A_H is the effective Hamaker coefficient representing the strength of polarization forces. Combining equation (3.6) and equation (3.7), d at thermodynamic equilibrium can be expressed as

$$d = \left(\frac{|A_H|}{6\pi\rho_l(\frac{q_m}{T_m}(T_m - T) + \frac{\rho_l - \rho_s}{\rho_l \rho_s}(P_m - P))} \right)^{1/3}. \tag{3.8}$$

Dash et al. [42] have used a different notation where the derivative of the excess surface free energy was expressed as

$$\frac{\partial F_{total}}{\partial d} = \frac{3\Delta\gamma\sigma^2}{d^3}, \tag{3.9}$$

where σ is a constant on the order of a molecular diameter, and $\Delta\gamma$ is the difference between the coefficients of dry and wetted interfaces:

$$\Delta\gamma = \gamma_{lv} + \gamma_{sl} - \gamma_{sv}, \tag{3.10}$$

where subscript l is for liquid, v is for vapor, and s is for solid. Combining equation (3.7) and (3.9), the Hamaker coefficient can be expressed as

$$A_H = 12\pi\Delta\gamma\sigma^2. \tag{3.11}$$

Figure 3.1 shows the predicted d as a function of temperature together with a dashed line indicating the molecular length of one water molecule. In this figure, $\Delta\gamma = -0.024$ J/m^2 [44] was used together with $\sigma = 2.8$ Å, yielding $A_H = -7.1 \cdot 10^{-20}$ J.

The displacement $\Delta\mu(T, P)$ can increase in the presence of impurities μ_s (for instance, salt [45]), by an electrostatic potential μ_e [43], or by damage at the interface μ_D due to a collision [41]. Wåhlin and Klein-Paste [45] have expressed the chemical potential due to salt as

$$\mu_s = k_b T \ln(\alpha_w), \tag{3.12}$$

where k_b is the Boltzmann constant, and α_w is the activity of the solution. An electrostatic potential can be present when there is an ionic solution, and Thomson [43] has derived that

$$\mu_e = \frac{q_s^2}{\kappa\epsilon\epsilon_0}\big(1 - \frac{1}{\kappa d}\big)\exp(-\kappa d), \tag{3.13}$$

where κ^{-1} is the Debye length, ϵ, is the dielectric constant, ϵ_0, is the permittivity of free space, and q_s is the surface charge. Wettlaufer [46] has proposed that μ_D can be expressed as a fraction ξ of the kinetic energy at impact, E_i, acting over the mass $\rho_l \pi a_d^2 d$ of damage, i.e:

$$\mu_D = \frac{\xi E_i}{\rho_l \pi a_d^2 d}, \tag{3.14}$$

where a_d is the maximum contact radius in the collision and is dependent on V_i. The damage term is used to describe how microscopic and mesoscopic changes lead to the deterioration of macroscopic material properties. With

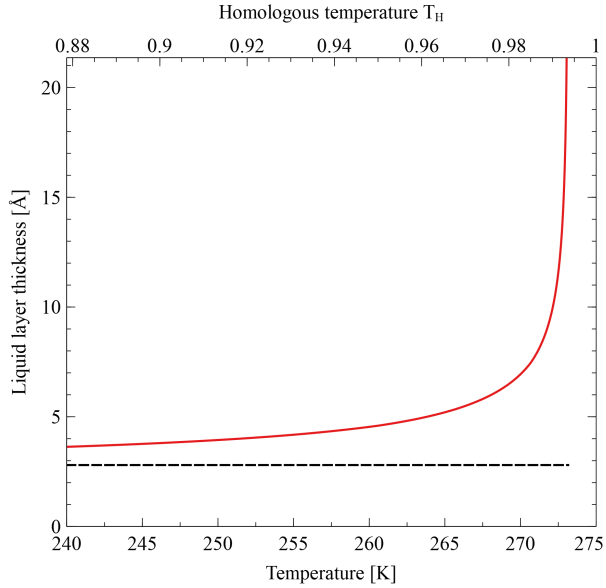

Figure 3.1: Calculation of the QLL thickness d on ice as a function of temperature T. The red solid line shows the calculated d. The dashed black line shows 2.8 Å, illustrating the molecular length of a water molecule.

these expressions for the chemical potentials, the displacement $\Delta\mu(T,P)$ can be expressed in a general equation as

$$\Delta\mu(T,P) = -\frac{A_H}{6\pi\rho_l d^3} + k_b T\ln(\alpha_w) + \frac{\xi E_i}{\rho_l \pi a_d^2 d} + \frac{q_s^2}{\kappa\epsilon\epsilon_0}\left(1-\frac{1}{\kappa d}\right)\exp(-\kappa d), \tag{3.15}$$

$$= \frac{q_m}{T_m}(T_m - T) + \frac{\rho_l - \rho_s}{\rho_l\rho_s}(P_m - P). \tag{3.16}$$

In the same way as for equation (3.8), this equation can be solved for d given a certain impurity and/or collisional damage. This general equation can be used for snow when predicting how much of it will melt due to added salt or to predict the de-icing of a surface caused by electrostatic potential.

Dash et al [41] and Wettlaufer [46] have previously shown that μ_D becomes dominant in equation (3.15) already for low values of damage if there are no impurities and no ionic solution present ($\mu_s = 0$ and $\mu_e = 0$), and if damage at the interface was caused by a collision. Hence, the solution with respect to d can be expressed as [46]

$$d = \frac{\xi E_i}{\pi\rho_l a_d^2}\frac{1}{\left(\frac{q_m}{T_m}(T_m - T) + \frac{\rho_l-\rho_s}{\rho_l\rho_s}(P_m - P)\right)}. \tag{3.17}$$

3.3 Sintering of ice

Sintering is a thermodynamic process in which bond strength grows over time and is commonly observed for metals and ceramics [47]. For ice with the high

values of T_H that naturally occur in an earth environment, it is not surprising that sintering is a commonly observed phenomenon for ice particles in contact with each other and has been extensively studied for ice and snow [48, 49]. The sintering bond for ice forms as a grain boundary groove geometry, which was first shown by Colbeck [48], before this it was incorrectly believed that the geometry could be described as a concave bond similar to a liquid bridge. This bond formation is contact-time dependent, and the speed of growth is temperature dependent [48]. A general regime map for any sintering material has been presented by Li et al. [50]. It describes different contact regimes. In this work, the initial phase of sintering for short contact times was found to be dominated by adhesive-elastic interaction (the JKR model), while longer contact times were dominated by other contact regimes.

3.4 Higa et al experimental study

Higa et al. [51] have conducted an extensive study of ice particles colliding with ice walls at different temperatures and for different particle sizes. The study focused on determining e_n and one of the key findings in this work was that e_n drastically starts to decrease for V_i above a certain threshold velocity V_c. The authors have proposed an empirical model for e_n as

$$e_n = \begin{cases} e_{qe}\left(\frac{V_i}{V_c}\right)^{-\ln(V_i/V_c)} & V_i \geq V_c, \\ e_{qe} & V_i < V_c, \end{cases} \tag{3.18}$$

where e_{qe} is the so-called quasi-static, e_n, which means the value of e_n when it seems independent of V_i. The study reported that V_c is dependent on R, and an empirical equation has been proposed by Higa et al. [51], which is simplified in this thesis and is expressed as

$$V_c = K_1 \exp\left(\frac{K_2}{k_b T}\right) R^{-0.5}, \tag{3.19}$$

valid for $T > 229K$, where $K_1 = 7.055 \cdot 10^{-7}$ and $K_2 = 0.25$ are the resulting constants based on the best fit of the experimental measurements performed in the study by Higa et al. [51].

Chapter 4

Scientific approach

4.1 Numerical implementations for dry snow adhesion modeling

Dry snow adhesion was studied in Paper I, by simulating ice particles and agglomerates of ice particles colliding with massive walls in the normal direction. In this context dry snow is referred to as ice sufficiently cold, so that premelting can be neglected. The material properties were chosen to represent $T = 261$ K. The predicted premelted liquid layer at this temperature is less than two diameters of a water molecule (Figure 3.1). Based on the regime map of sintering mentioned in chapter 3.3, it was assumed that the collisional time and the time of contact between ice particles were sufficiently short so that the contact was JKR dominated. Three different scenarios of impacts were studied: single particle, small agglomerates, and large agglomerates. The simulations were performed in LIGGGHTS, which is an open-source software [52]. LIGGGHTS uses a soft-sphere approach (DEM) to simulate the contact between particles by allowing them to overlap, and contact forces are therefore expressed as functions of overlap. The JKR model was used where the governing equations, equation (2.9) and (2.10), were implemented into LIGGGHTS. The model was implemented using a lookup table for $F_n(\delta)$ to speed up the simulations, a technique used in previous studies [21]. The implementation of the model also accounted for negative overlaps after contact, and it was verified that the energy loss for a particle rebounding after a collision with a wall is same as equation (2.14).

No treatment for the adhesive sliding and rolling of particles exists in LIGGGHTS, and therefore, this was implemented. For sliding this was done by implementing equation (2.21). A constant directional torque (CDT) model was used for rolling to model the adhesive resistance for rolling. The CDT model uses a resistance torque, M_r, in the opposite direction of the relative torque, ω_{rel}, defined as

$$M_r = -\frac{\omega_{rel}}{|\omega_{rel}|} f_r k_n \delta_n R^*, \tag{4.1}$$

where f_r is the rolling coefficient, and k_n is an elastic spring variable defined as

$$k_n = \frac{4}{3}E^* a. \tag{4.2}$$

A challenge to use the CDT model is that f_r is not well defined. Often the value of f_r is calibrated based on angle of repose experiments [53], however, angle of repose experiments are more complex for adhesive particles since the angle depends on the intermolecular interaction in the contact.

Dominik and Tielens [54] have derived for the DT model that the energy lost for an adhesive particle in equilibrium contact ($a \approx a_0$) rolling πR^* (which is equivalent of a rotation of 90° between two particles [54]) is given by

$$E_{roll} = 3\pi^2 W \delta_{r,c} R^* = \frac{\pi^2 W a_0 R^*}{4}\frac{\Delta\gamma}{\gamma}. \tag{4.3}$$

The corresponding energy loss for the CDT model is simply the torque multiplied by radians of a rotation. Assuming that the contact is at equilibrium, $a \approx a_0$, it follows that

$$E_{roll} = f_r k_0 \delta_0 R^* \left(\frac{\pi}{2}\right) = f_r \underbrace{\frac{4}{3}E^* a_0}_{k_0} \underbrace{\frac{2(6^{1/3})}{3}\frac{a_0^2}{2(6^{1/3})R^*}}_{\delta_0} R^* \frac{\pi}{2} \tag{4.4}$$

$$= \frac{2\pi f_r a_0^3 E^*}{9}. \tag{4.5}$$

By setting equation (4.3) and equation (4.5) equal, one can derive the value f_r must have for the CDT and the DT models to have the same energy dissipation:

$$f_r = \frac{9}{2\pi a_0^3 E^*}\frac{\pi^2 W a_0 R^*}{4}\frac{\Delta\gamma}{\gamma} \tag{4.6}$$

$$= \frac{1}{4a_o^2 R^*}\underbrace{\left(\frac{9\pi W R^{*2}}{2E^*}\right)}_{a_0^3}\frac{\Delta\gamma}{\gamma} \tag{4.7}$$

$$= \frac{a_0}{4R^*}\frac{\Delta\gamma}{\gamma}. \tag{4.8}$$

In this format f_r becomes dependent on R^*, $\Delta\gamma/\gamma$, and the adhesive-elastic properties that define a_0. This approach to calculate f_r was implemented in the code.

4.1.1 Agglomerate formation and computational setup for agglomerates

Agglomerates of different sizes can easily form in a turbulent field with many cohesive particles. Both small and large agglomerates were formed in Paper I and simulated to collide with massive walls where the aim with the analysis was to find the stick velocity for an agglomerate by varying V_i. The small agglomerates consisted of two, three, four, and five particles, while the large agglomerates consisted of 1000 particles. All agglomerates had a uniform

particle size of $R = 25$ μm since this was reported in [6] to be the most common size of spherical ice particles adhering to a vehicle surface in an in-field test. The threshold was chosen so that if 90% of the particles in an agglomerate stuck to the wall, the agglomerate was considered to stick, and the corresponding V_i was, therefore, less or equal to V_s. Since the small agglomerates had a maximum of five particles, all particles for the small agglomerates were included and consequently, this threshold only applied to large agglomerates. For both agglomerate types, it was assumed that the contact between particles was sufficiently long so that the contact stabilized with a contact radius $a = a_0$. Initialization simulations were performed to achieve this numerically, where velocity-dependent damping was introduced into this simulation so that the particles stabilized around $F_n = 0$. It was assumed that small agglomerates were formed by close packing while the large agglomerates were formed by more loose packing. The packing of an agglomerates can be related to the coordination number Z which is defined as, [19]

$$Z = \frac{2C}{N - N_0}, \tag{4.9}$$

where N_0 is the number of particles with no contacts, N is the number of particles and C is the number of particle-particle contacts.

The small agglomerates were formed by placing them as closely packed together as possible. Since these agglomerates are asymmetric, how they are oriented in space relative to the wall will influence the energy loss in a collision with a wall. We therefore explored the effect of asymmetry by repeating collisions between the small agglomerates and a wall for different orientations. The rotations were done on the two axes that are orthogonal to the impact vector (i.e. the axes that span up the impact wall plane), and rotations were done in steps of $\pi/100$ radians from 0 to $\pi/2$. This led to a total of 51 orientations per axis and 1326 orientations for each agglomerate.

The large agglomerates were formed using a method similar to the one used by Tamadondar et al. [55]. First, the particles were randomly inserted into a large domain, then a centripetal gravity field was applied at the center of the domain so that the particles were slowly dragged into the center. The simulation then continued until the particles had dissipated away all kinetic energy and stabilized the contacts.

4.2 Material properties

A considerable amount of the analyses in this thesis is depended on estimations of material properties. These were not always trivial to obtain especially since they can be temperature-dependent. The work of adhesion W and the effective Young modulus E^* of the interaction properties were particularly important parameters since they define adhesive-elastic interactions. W was estimated by using equation (2.7) with found literature values for surface energies as the input. Similarly, E^* was estimated by finding values of ν and E for each material investigated. The ν for ice has been reported to be independent of temperature in Gold [56], and this assumption was made in the present study. The Young modulus for ice was calculated based on temperature dependency

as [57]

$$E = \frac{10^{11}}{10.40(1 + 1.07 \cdot 10^{-3}(T - 273.15) + 1.87 \cdot 10^{-6}(T - 273.15)^2}, \quad (4.10)$$

where the temperature T is in units of Kelvin. E based on equation (4.10) only changed weakly with temperature, for example, $E(263K) = 9.67$ GPa, while $E(253K) = 9.98$ GPa.

The parameter $\Delta\gamma/\gamma$ for ice particles was calculated based on the experimental values for the critical rolling force F_{cr} obtained by Gundlach et al. [58] for ice. F_{cr} was found to be 11.48 mN for equal-sized particles in contact with $R = 1.45\mu m$. F_{cr} was related to $\Delta\gamma/\gamma$ as

$$F_{Roll} = 3\pi W \delta_{r,c} = \frac{\pi W a_0}{4} \frac{\Delta\gamma}{\gamma}, \quad (4.11)$$

and, based on this, $\Delta\gamma/\gamma \approx 1$ was obtained for ice particles.

Walls of the materials ice, hardened glass, steel, and ABS polymer were studied in Paper I while walls of the materials ice, hardened glass, and ABS polymer were studied in Paper II.

4.3 Ice particle experiments

In Paper II, e_n for millimeter-sized ice particles colliding with massive walls was measured. Ice particles were created by dropping a mixture of water and food colorant into liquid nitrogen with a syringe. This method of creating ice particles has been used previously by Vargas et al [59]. The syringe needle used was the smallest available, and this needle size defined the size of the ice particles. Each particle was picked up gently using a paintbrush, and the particles were released into a vertical metal pipe. The particles then accelerated due to gravity and collided with the massive wall at a certain impact velocity, V_i. The course of the collision was recorded using a high-speed camera at 4000 frames per second, and the recording began when a laser beam detected a particle outside the metal pipe. The experiments were performed in a large cooling chamber where the temperature could be controlled, and a temperature probe located 20 cm from the massive wall was used to monitor the temperature. One standard deviation from the mean was interpreted as temperature uncertainty. The experimental setup is shown in Figure 4.1.

The recorded sequence of images for a collision was then analyzed using the software Fiji and the particle tracking plugin TrackMate [60]. Before analyzing the images, the images were pre-processed in Fiji to improve particle detection by removing gradient backgrounds, image segmentation, and filling holes obtained from the segmentation where holes can occur because of light reflections in particles. The particle radius of each frame in a collision sequence was calculated by adding the pixel area of every pixel in the segmented sphere. The overall particle radius for a collision was then calculated as the median of the obtained radii in a collision, where the median was used instead of the average to remove outliers caused by edge effects. Output for the trajectory points before and after collision was taken from TrackMate. These points were then post-processed to calculate the corresponding velocity before and

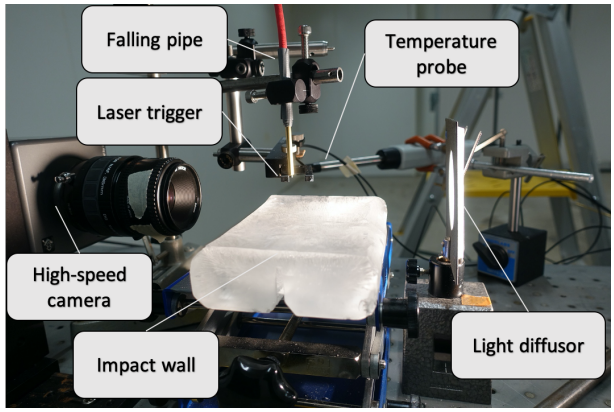

Figure 4.1: Photograph of the experimental setup.

after collision. The uncertainty of the center position, δx, for a particle was quantified by manually measuring the center points. The average difference between this manual measurement and the output from TrackMate was taken as δx. $\delta x = 26.13$ μm was obtained, which propagates to a velocity uncertainty of $\delta V = 4000 \cdot 26.13 \cdot 10^{-6} = 0.105$ m/s. The uncertainty of the coefficient of restitution, δe_n, was then calculated based on the propagation of uncertainties as

$$\delta e_n = \sqrt{\left(\frac{\delta V_i}{V_i}\right)^2 + \left(\frac{\delta V_r}{V_r}\right)^2} e_n. \tag{4.12}$$

Paper II focused on normal collisions, and collisions recorded with a clear tangential impact were removed from the data set.

Chapter 5

Ice particles colliding with massive walls

5.1 Elastic-adhesive collisions for dry snow (Paper I)

The JKR model in Chapter 2.2, showed that a certain amount of energy, E_s, is required for a particle to rebound from a particle-wall collision. The theory predicts this energy to be constant, and a certain threshold velocity, V_s, which a particle will adhere if $V_i \leq V_s$, can be calculated based on E_s. The e_n increases for velocities above V_s, as shown in Figure 2.3 (equation (2.20)). Figure 5.1 shows the theoretical predicted V_s for ice particles colliding with massive walls of different materials as a function of R.

The V_s obtained for small and large agglomerate impacts increased with increasing coordination number. The maximum V_s obtained for ice agglomerates colliding with a polymer wall is shown in Figure 5.2 as a function of coordination number. This trend of increasing V_s with increasing coordination number can be explained by the increase in the possible tangential movement of particles and, subsequently, the increased in energy loss caused by tangential interactions. This is a substantial increase in energy loss, for example, the large agglomerate (with 1000 particles) adhered at a velocity of 0.5 m/s which then had a kinetic energy that was almost 80,0000 times higher than what a single ice particle has when colliding with a polymer wall at $V_s = 0.056$ m/s. It is worth emphasizing that the analysis with agglomerate impacts was sensitive to how tangential sliding and rolling were modeled because the energy dissipation was so dependent on tangential dissipation caused by sliding and rolling.

5.2 Collisional melting model (Paper II)

Paper II, presents the experimental measurements of ice particles colliding with different massive walls. The reader is referred to Paper II for the results of these measurements. The results of these measurements were used to develop a new collisional melting model.

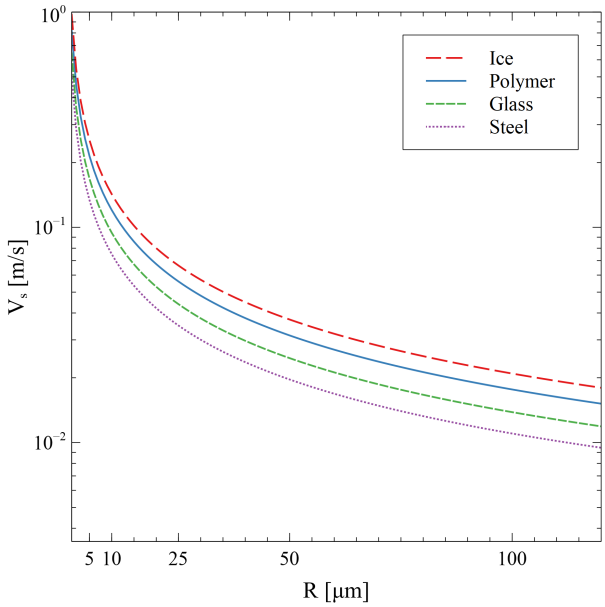

Figure 5.1: Analytical V_s for single ice particles colliding with massive walls of different materials as a function of R for $T = 261K$.

Wettlaufer [46] has proposed a collisional melting/fusion model for collisions between ice particles, where the predicted QLL thickness d is dependent on the collision. This equation was simplified for ice particles colliding with a massive wall in the present study and the derivation is shown in Appendix A. The QLL thickness, d, caused by an increase in premelting as a result of the damage to the ice particle when it collides with a massive wall, can be expressed as

$$d = \left(\frac{16\sqrt{6}E^*}{135\pi}\right)^{2/5} \frac{\xi R \rho_s^{3/5} V_i^{6/5}}{\left(\frac{\rho_l q_m}{T_m}(T_m - T) + \frac{\rho_l - \rho_s}{\rho_s}\left(P_m - \xi\left(\frac{40}{\pi^4}\rho_s V_i^2 E^{*4}\right)^{1/5}\right)\right)}. \tag{5.1}$$

This simplified format directly shows that d is proportional to $E^{*2/5}$ and R. Wettlaufer [46] has bounded $\xi \in [0.1, 0.2]$ based on the experimental results by Higa et al. [51]. Figure 5.3 shows the predicted d/R as a function of V_i for an ice particle colliding with an ice wall at $T = 261$ K. The figure plots the established solution presented in equation (5.1) (green dotted line) and the general solution with contributions from intermolecular forces and the damage contribution as shown in equations (3.15) and (3.16) (solid blue line). As can be seen in Figure 5.3, there was a difference between the two solutions for the lower V_i only and we could conclude that the damage term was dominant for a sufficiently high V_i, which has previously been shown [41, 46].

A previous experimental study (see Chapter 3.4) has shown that the energy loss an ice particle colliding with a massive wall rapidly increases with increasing V_i when $V_i \geq V_c$ for some critical velocity V_c [51]. The study in Paper II confirmed this finding for ice particles with lower particle size than previously

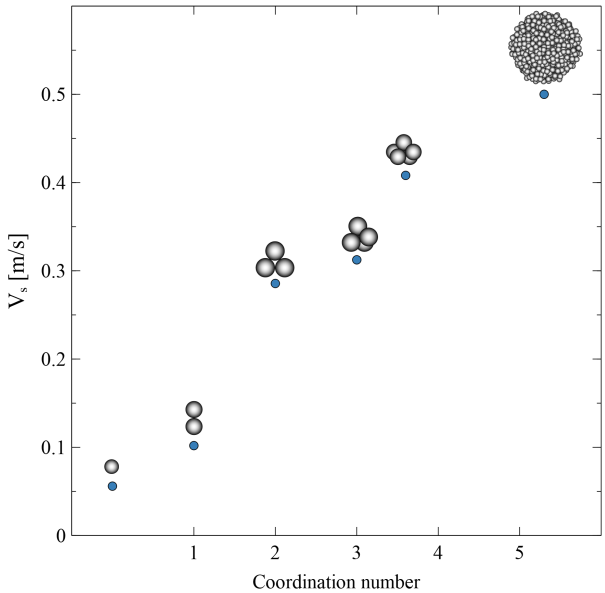

Figure 5.2: Maximum V_s obtained for agglomerates of ice particles colliding with a polymer wall as a function of coordination number.

measured before ($R = 0.82$ mm). The empirical equation (3.18) gives that $e_n \propto V_i^{-\ln(V_i/Vc)}$, the proportionality of which is similar to $e_n \propto V_i^{-1}$ and consequently, it is significantly more sensitive to changes in V_i than the plastic dissipation model mentioned in Chapter 2.3, where $e_n \propto V_i^{-1/4}$. Therefore, plastic dissipation models cannot model this fast increase in energy loss with increasing V_i. Given that these models assume relatively low T_H and do not account for any effects on melting, this is maybe not surprising. Studies have, however, shown that e_n can be sensitive to high values of T_H. A recent study of steel balls colliding with a heated metal wall has shown that e_n started to decrease as early as $T_H > 0.6$ [61]. Another study of glass particles colliding with a poly ethylene glycol substrate has reported that e_n fell to zero as the substrate approached the melting point. It has also been shown that e_n for micrometer-sized metal particles stops following $e_n \propto V_i^{-1/4}$ and instead follows $e_n \propto V_i^{-1}$ at sufficiently high V_i [62].

As predicted by equation (5.1), a particle colliding with a wall at a sufficiently high speed can experience locally increased premelting caused by a shift in chemical potential. This can increase energy losses. There is a loss in the amount of kinetic energy that causes damage at the interface ξE_i. There is also a liquid layer in the collision. The presence of this layer can cause an energy loss due to capillary adhesion of a particle colliding with a wall (Chapter 2.4). Only viscous damping can capture the velocity dependency seen for ice particles since the other contributions caused by capillary adhesion (i.e. the static contact contributions) are not velocity-dependent.

An integration as shown in equation (2.29) must be performed to establish an analytical solution for the energy loss caused by viscous damping, E_v. With

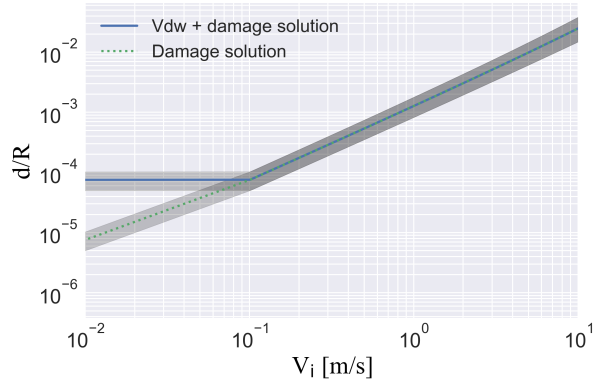

Figure 5.3: Predicted d/R as a function of V_i for an ice particle colliding with an ice wall at $T = 261$ K. The blue solid line shows the solution with the damage term and the intermolecular term (abbreviated Vdw). The green dotted line shows the solution with only the damage term. $\xi = 0.15$, was used and the shaded area shows the variation for $\xi = 0.15 \pm 0.05$

a predicted, E_v, the e_n caused by viscous damping can be expressed as

$$e_n = \sqrt{\frac{E_i - E_v - \xi E_i}{E_i}}, \tag{5.2}$$

where ξE_i is the amount of damage at the interface. However, for a premelted quasi-liquid layer the function $h(x)$ in equation (2.26) is unknown, and the liquid layer will increase in thickness up to d during the collision. It is, however, reasonable to expect that the resulting E_v will be similar to equation (2.30) but with another dependency on d/ε. Therefore, it was argued in paper II that $E_v \propto (d/\varepsilon)^{a/b}$ for some fraction, a/b, where a and b are unknown integers. It was found that $a/b = 3/2$ best capture $e_n \propto V_i^{-1}$ using equation (5.2). η is also unknown for the premelted liquid layer caused by the collision, but the viscosity for a liquid is generally expected to be dependent on temperature, as

$$\eta \propto \exp\left(\frac{G_0^+}{k_b T}\right), \tag{5.3}$$

where G_0^+ is a potential energy barrier often found by experimental fitting to experimental data [63]. Based on this, we proposed that

$$E_v = C \exp^{\frac{G_0^+}{k_b T}} V_i R^2 (d/\varepsilon)^{3/2}, \tag{5.4}$$

where C is a constant representing all linear constant terms with unit Pa· s. A non-linear least-squares fit was performed using the experimental measurements in Paper II as input to obtain the values for C and G_0^+. This fit was done for both T = 267 K and T = 254 K so that they could be compared, and remarkably similar values of C and G_0^+ were obtained. The average values of the unknowns were found to be $C = 0.5 \cdot 10^{-10}$ Pa·s and $G_0^+ = 0.5$ eV, and the best fit at different temperatures only varied by 0.6% and 0.5% for C and G_0^+.

Using these values for C and G_0^+, the e_n caused by collisional melting can be predicted using equation (5.2) and compared to the experimental measurements. Figure 5.4 shows the predicted e_n as lines for ice particles colliding with massive walls of ice, polymer, and hardened glass. As can be seen in the figure, the new e_n captures the velocity trend observed in the experiments, temperature trends, and the difference between wall materials.

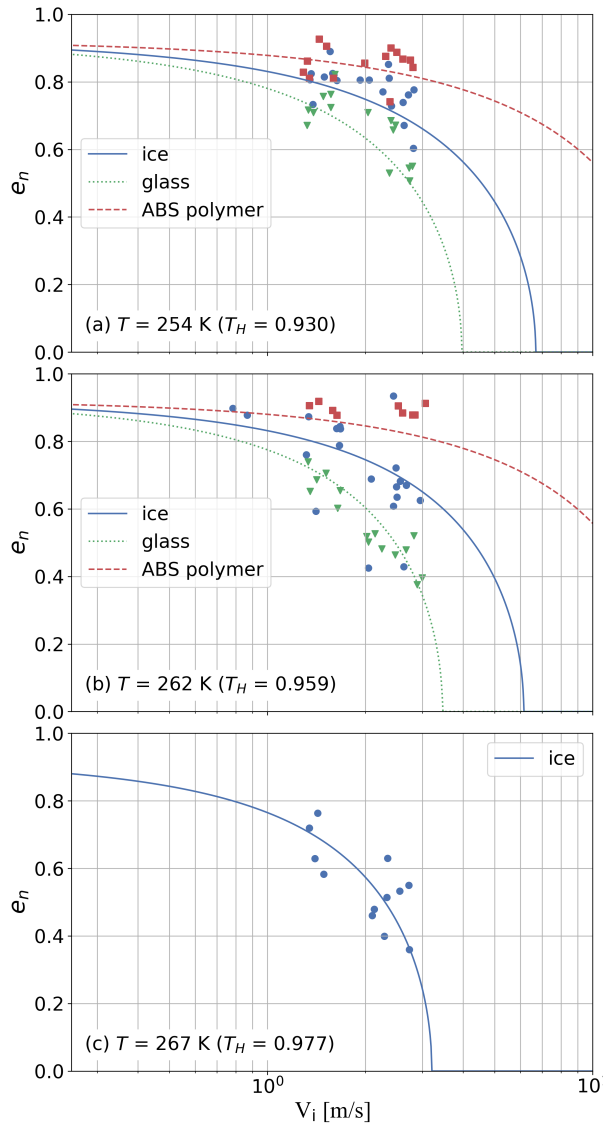

Figure 5.4: The e_n for ice particles with $R = 0.82$ mm colliding with different massive walls as a function of V_i. Solid, dashed, and dotted lines show the predicted e_n caused by collisional melting for ice particles colliding with an ice wall, a polymer wall, and a glass wall, respectively. Marker symbols (circle, square, and triangle) show experimental measurements for ice particles colliding with an ice wall, a polymer wall, and a glass wall.

5.3 Regime map for ice particles

The combined work of Papers I and II predicts that the velocity of impact has a very nonlinear influence on the energy dissipation and the e_n for an ice particle colliding with a massive wall. A regime map of e_n can be created by combining the effect of adhesive-elastic interactions Paper I with the collisional melting in Paper II. This can simply be done by combining the coefficient of restitution from the JKR model e_{JKR} with the coefficient of restitution from the collisional melting e_{cm}. Multiple coefficients of restitution can be combined by multiplying different contributions as [27]

$$e_n = \prod_i e_i \tag{5.5}$$

The combined e_n for an ice particle colliding with a massive wall is shown in Figure 5.5.

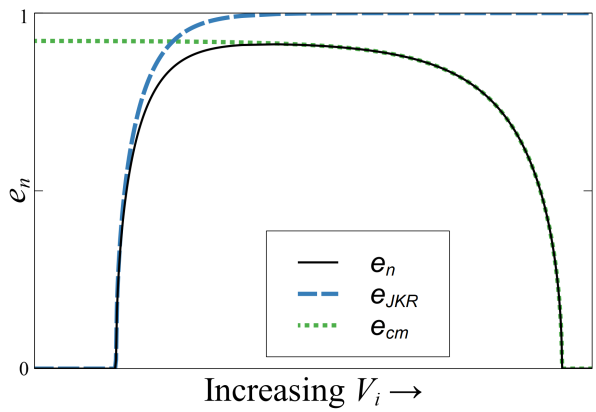

Figure 5.5: The coefficient of restitution for ice particles upon collision with a massive wall. The blue dashed line shows the coefficient of restitution from adhesive-elastic interaction e_{JKR} (using the JKR model). The green dotted line shows the coefficient of restitution from collisional melting e_{cm}. The black solid line (e_n) shows the combined coefficient of restitution.

Particles are expected to adhere to the wall after collisions at low velocities ($V_i < V_s$). The e_n will increase with increasing V_i up to a local maximum and will obtain a quasi-stable value. An additional increase in V_i will cause the e_n to suddenly start to decrease down to zero again. After sticking at increased velocities, it is likely that the particles again starts to rebound due to fragmentation, and e_n then becomes less well defined.

5.3.1 Effect of wall material

One of the objectives of this thesis was to analyze how the material properties of vehicle surfaces affect snow adhesion. Two key interaction properties were identified in the models: The work of adhesion W and the effective Young's modulus E^*. The proposed regime map for e_n that combines adhesive-elastic

interactions with collisional melting predicts different dependencies for the collisional energy loss with E^*. Figure 5.6 shows the combined e_n as a function of V_i for ice particles colliding with different massive walls. The e_n was calculated for particles with $R = 100$ μm at $T = 261$ K. The energy loss associated with low velocity impact in a collision, E_s, is proportional to $W^{5/3}E^{*-2/3}$, therefore, particle-wall interactions with **high** E^*, e.g. when the wall is glass, will yield low losses in a collision. In contrast, the energy loss E_v of high-velocity impacts is proportional to $E^{*4/5}$, which means that particle-wall interactions with **low** E^*, such as for a polymer wall, will have lower losses. This gives a complex dependency on the optimal wall material for avoiding snow accumulation since the dependency is also affected by velocity. These results imply that it might be beneficial to have a sensor cover of different materials, depending on where on the vehicle the sensor is located. For example, for the radar cover at the front of a car, one would expect high-velocity collisions similar to the speed of the vehicle, and thus a material that yields a low E^* might be beneficial, while in the rear wake of the car, a sensor cover should instead have a material that yields a high E^*.

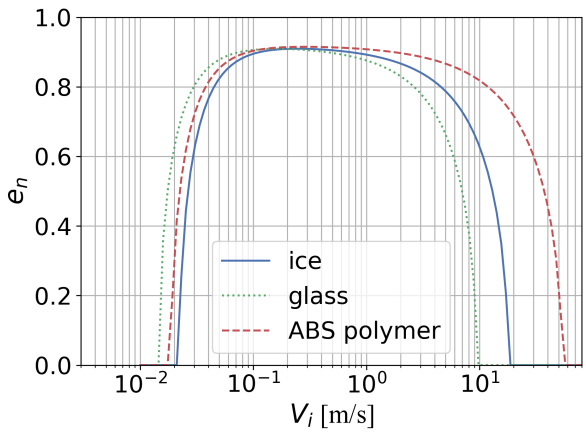

Figure 5.6: The combined e_n for ice particles colliding with different massive walls as a function of V_i for $R = 100$ μm and $T = 261$ K. Solid, dashed, and dotted lines show the predicted e_n for ice particles colliding with an ice wall, a polymer wall, and a glass wall, respectively.

5.3.2 Temperature dependency

The model for collisional melting in Paper II depends on temperature. Greater melting of a liquid layer is expected at higher temperatures, and the resulting viscous damping is predicted by the model to be higher at higher temperatures even though the contribution from viscosity decreases with temperature. Paper I discusses dry snow adhesion at a cold enough fixed temperature where the effects of a liquid layer in equilibrium is assumed to be negligible. This assumption is likely not valid for higher temperatures and a temperature dependent work of adhesion W most likely needs to be introduced for these high temperatures. W

will likely increase with increased temperature since there should be a thicker premelted liquid layer at higher temperatures, especially for $T > 263$ K. Figure 5.7 shows e_n for ice particles colliding with an ice wall at different temperatures. Since e_{JKR} is unknown for $T > 263$, only $T = 261$ K was plotted for this low-velocity regime. V_s is expected to increase with increasing T, causing the range of lower velocities where $e_n = 0$ to increase and, consequently, the range of nonzero values of e_n will decrease with increasing T.

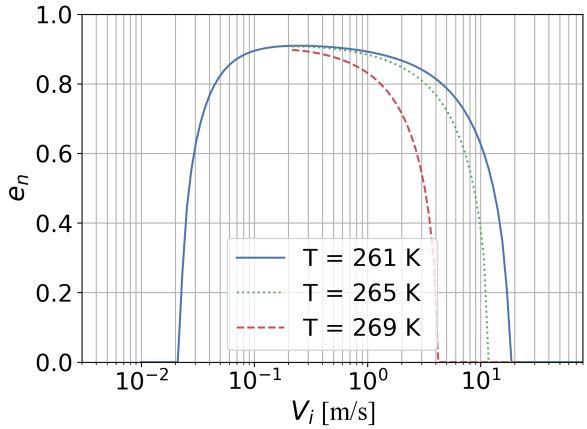

Figure 5.7: The combined e_n for ice particles colliding with a massive ice wall as a function of V_i for $R = 100$ μm. Solid, dotted, and dashed lines show the e_n predicted for the temperatures $T = 261$ K, $T = 265$ K, and $T = 269$ K, respectively.

Chapter 6

Summary of papers

6.1 Paper I

Aim: Examine at which velocities dry ice particles and agglomerates of ice particles are theoretically expected to stick during a normal collision with a massive wall.

Summary: A computational framework was used combining three contact models: The JKR model in the normal direction, the adhesive sliding model as used by Marshall [21], and a novel rolling model, where the resistance of rolling was assumed to be due to adhesion. The paper reports on an analytical solution to single-particle collisions combined with simulations of small and large agglomerates. The analysis predicts that single-ice particles are more likely to adhere to a polymer wall than a glass or steel wall, and the effective Young's modulus, E^*, is an important interaction property. It was also found that the maximum obtained stick velocity increased with increased coordination number in an agglomerate. This was explained by the higher amount of energy losses caused by sliding and rolling at the impact, and the increase in energy loss is significant compared to the increased kinetic energy.

6.2 Paper II

Aim: To study the coefficient of restitution, e_n, of millimeter-sized ice particles and propose a novel collisional melting model.

Summary: Experiments on millimeter-sized ice particles colliding with massive walls were performed. Different temperatures and different wall material properties were used. It was found that the obtained velocity-dependency was similar to what was obtained in another experimental study [51] for larger particles. It was also found that the different wall materials yielded different e_n, where the hardened glass had the lowest values of e_n, and a polymer had the highest.

Based on the experimental results, the previous experimental study by [51], and a study proposing a model for collisional fusion [46], a novel model for e_n of ice particles was proposed, where the damping in a collision was explained by collisional premelting of a liquid layer and viscous damping caused by this premelted liquid layer. This model was found to capture the obtained temperature dependency and the material dependencies obtained with the experiments. The size dependency of e_n presented by Higa et al. [51] was also captured by the novel model.

Chapter 7

Conclusions

The objectives of this study were to derive computational models for ice particles colliding with massive walls and analyze the dependencies of material properties and temperature. A velocity-dependent regime map for the energy dissipation in these impacts was derived, where two dominating regimes were identified: adhesive-elastic interactions and collisional melting. The adhesive-elastic interactions were caused by van der Waals forces and were modeled using the JKR model. This regime dominated at low-velocities of impact, while collisional melting occurred at higher velocities, where damage at the interface was caused by the collision, subsequently causing a shift in chemical potential and an increase in the premelted liquid layer. The premelted liquid layer then caused viscous damping of the ice particle at impact, which increased energy dissipation at impact.

Three different wall materials were compared for the two velocity regimes in the thesis: ice, polymer, and glass. The energy loss at impact for the adhesive-elastic regime was expected to be the highest for ice and the lowest for glass, and the energy loss for the collisional melting regime was expected to be the highest for glass and the lowest for the polymer wall. This differences between the two regimes was explained by the energy loss having different dependencies on the effective Young's modulus, E^*, which for the adhesive-elastic regime is proportional to $E^{*-2/3}$, and for the collisional melting regime is proportional to $E^{*3/5}$. These results imply that the same material can be efficient to avoid snow accumulation and to stimulate it depending on the velocity regime of impact at which the snow hits the surface. For example, a material with high E^* can be effective against snow accumulation at the rear of a car, where a large aerodynamic wake is present, but the same material could be ineffective at the front of the car where high velocities of impact are expected to occur. The material properties representing the interaction in a collision between an ice particle and a vehicle surface can also quickly change to the properties of ice either through a buildup on an ice wall caused by deposition (a phase change from vapor to solid ice), or through an accumulation of snow that forms an ice wall with high roughness.

Chapter 8

Future work

Many open research questions remain to resolve the problem of snow accumulating on vehicle surfaces when driving on a snowy road. One of the obvious problems is how the work of adhesion changes as a function of temperature for temperatures where the premelted liquid layer can no longer be assumed to not affect a collision. Deriving an analytical solution to this problem might prove challenging, and a more reasonable next step would be to propose an empirical relationship based on experimental results. It is also well known that adhesion is roughness sensitive, which means that wall roughness should influence the work of adhesion, however, it is not obvious how to predict this influence without reliable experimental procedures.

This thesis only examined particles colliding with walls in a vacuum. However, a turbulent aerodynamic field surrounds a car when it moves in air at driving speeds of 70-90 km/h. This aerodynamic field governs the transportation of particles, which defines the impact velocities, and can push/peel away particles from surfaces that had previously adhered to the surface. This aerodynamic field must be incorporated into the mathematical modeling to fully predict snow contamination on cars. Experimental data on snow contamination on surfaces is required, so that aerodynamic simulations coupled with the collision model for ice particles can be validated.

Bibliography

[1] I. Isaksson-Hellman and M. Lindman, "Using insurance claims data to evaluate the collision-avoidance and crash-mitigating effects of Collision Warning and Brake Support Combined with Adaptive Cruise Control," *IEEE Intelligent Vehicles Symposium, Proceedings*, vol. 2016-Augus, no. Iv, pp. 1173–1178, 2016.

[2] E. Martí, M. Á. De Miguel, F. García, and J. Pérez, "A Review of Sensor Technologies for Perception in Automated Driving," *IEEE Intelligent Transportation Systems Magazine*, vol. 11, no. 4, pp. 94–108, 2019.

[3] M. Jokela, M. Kutila, and P. Pyykönen, "Testing and validation of automotive point-cloud sensors in adverse weather conditions," *Applied Sciences (Switzerland)*, vol. 9, no. 11, 2019.

[4] U. department of Transporation, "FHWA Road Weather Management," 2020. [Online]. Available: https://ops.fhwa.dot.gov/weather/weather{_}events/snow{_}ice.htm

[5] IACS, "The international Classification for seasonal snow on the ground," *Prepared by the ICSI-UCCS-IACS Working Group on Snow Classification*, 2009.

[6] P. Abrahamsson, M. Eng, and A. Rasmuson, "An infield study of road snow properties related to snow-car adhesion and snow smoke," *Cold Regions Science and Technology*, vol. 145, pp. 32–39, 2018.

[7] K. G. Libbrecht, "Physical Dynamics of Ice Crystal Growth," *Annual Review of Materials Research*, vol. 47, pp. 271–295, 2017.

[8] B. R. Mcauliffe, "Potential for the Accumulation of Ice and Snow for a Boat-Tail Equipped Heavy-Duty Vehicle," *SAE Technical Paper*, no. 2016-01-8141, 2016.

[9] J. Wang, J. Zhang, Y. Zhang, F. Xie, S. Krajnović, and G. Gao, "Impact of bogie cavity shapes and operational environment on snow accumulating on the bogies of high-speed trains," *Journal of Wind Engineering and Industrial Aerodynamics*, vol. 176, no. May 2018, pp. 211–224, 2018.

[10] C. Huber, B. Weigand, H. Reister, and T. Binner, "Modeling and Numerical Calculation of Snow Particles Entering the Air Intake of an Automobile," *SAE International Journal of Passenger Cars - Mechanical Systems*, vol. 8, no. 2, pp. 538–545, 2015.

[11] K. Yoshitake, N. Kuratani, F. Nucera, A. Nikami, and A. Takamura, "Prediction Method of Snow Ingress Amount into the Engine Air Intake Duct Employing LES and Detailed Snow Accumulation Model," *SAE Technical Paper Series*, vol. 1, pp. 1–10, 2019.

[12] K. Daisuke, M. Yukiko, and T. Masao, "Micromeritical Porperties of Snow," in *International Conference on Low Temperature Science. I. Conference on Physics of Snow and Ice, II. Conference on Cryobiology*, 1967.

[13] H. H. Jellinek, "Liquid-like (transition) layer on ice," *Journal of Colloid And Interface Science*, vol. 25, no. 2, pp. 192–205, 1967.

[14] J. N. Israelachvili, *Intermolecular and Surface Forces.* New York: Academic Press, 1992.

[15] R. H. French, V. A. Parsegian, R. Podgornik, R. F. Rajter, A. Jagota, J. Luo, D. Asthagiri, M. K. Chaudhury, Y. M. Chiang, S. Granick, S. Kalinin, M. Kardar, R. Kjellander, D. C. Langreth, J. Lewis, S. Lustig, D. Wesolowski, J. S. Wettlaufer, W. Y. Ching, M. Finnis, F. Houlihan, O. A. Von Lilienfeld, C. J. Van Oss, and T. Zemb, "Long range interactions in nanoscale science," *Reviews of Modern Physics*, vol. 82, no. 2, pp. 1887–1944, 2010.

[16] V. Adrian Parsegian, *Van der Waals forces: A handbook for biologists, chemists, engineers, and physicists.* Cambridge University Press, jan 2005.

[17] F. M. Fowkes, "Attractive Forces At Interfaces," *Industrial & Engineering Chemistry*, vol. 56, no. 12, pp. 40–52, dec 1964.

[18] A. Chokshi, A. G. G. M. Tielens, and D. Hollenbach, "Dust Coagulation," *The Astrophysical Journal*, vol. 407, no. 2, pp. 806–819, 1993.

[19] C. Thornton, *Granular Dynamics, Contact Mechanics and Particle System Simulations: A DEM study.* Springer International Publishing, 2015, vol. 24.

[20] R. Moreno-Atanasio, "Energy dissipation in agglomerates during normal impact," *Powder Technology*, vol. 223, pp. 12–18, 2012. [Online]. Available: http://dx.doi.org/10.1016/j.powtec.2011.05.016

[21] J. Marshall, "Discrete-element modeling of particulate aerosol flow," *Journal of Computational Physics*, vol. 228, no. 5, pp. 1541–1561, 2009. [Online]. Available: http://dx.doi.org/10.1016/j.jcp.2008.10.035

[22] C. Dominik and A. G. Tielens, "Resistance to rolling in the adhesive contact of two elastic spheres," *Philosophical Magazine A*, vol. 72, no. 3, pp. 783–803, 1995.

[23] S. Krijt, C. Dominik, and G. M. Tielens, "Rolling friction of adhesive microspheres," *Journal of Physics D: Applied Physics J. Phys. D: Appl. Phys*, vol. 47, p. 9, 2014.

[24] C. Thornton and Z. Ning, "A theoretical model for the stick/bounce behaviour of adhesive, elastic- plastic spheres," *Powder Technology*, vol. 99, no. 2, pp. 154–162, 1998.

[25] M. J. Matthewson, "Adhesion of spheres by thin liquid films," *Philosophical Magazine A: Physics of Condensed Matter, Structure, Defects and Mechanical Properties*, vol. 57, no. 2, pp. 207–216, 1988.

[26] D. Y. Chan and R. G. Horn, "The drainage of thin liquid films between solid surfaces," *The Journal of Chemical Physics*, vol. 83, no. 10, pp. 5311–5324, 1985.

[27] V. S. Sutkar, N. G. Deen, J. T. Padding, J. A. Kuipers, V. Salikov, B. Crüger, S. Antonyuk, and S. Heinrich, "A novel approach to determine wet restitution coefficients through a unified correlation and energy analysis," *AIChE Journal*, vol. 61, no. 3, pp. 769–779, 2015.

[28] C. T. Corwe, J. D. Schwarzkopf, M. Sommerfeld, and T. Yutaka, *Multiphase Flows with Droplets and Particles*, 2nd ed. Taylor & Francis, 2012.

[29] S. C. Colbeck, "An overview of seasonal snow metamorphism," *Reviews of Geophysics and Space Physics*, vol. 20, no. 1, pp. 45–61, 1982.

[30] J. C. Berg, *An introduction to interfaces and colloids: The bridge to nanoscience*. World Scientific Publishing Co., jan 2009.

[31] N. Maeno, *Ice and Snow for Winter Sports*. Springer, 2016.

[32] B. J. Murray, D. O'Sullivan, J. D. Atkinson, and M. E. Webb, "Ice nucleation by particles immersed in supercooled cloud droplets," *Chemical Society Reviews*, vol. 41, no. 19, pp. 6519–6554, 2012.

[33] U. Nakaya, *Snow Crystals: Natural and Artificial*. Hardvard University Press, 1954.

[34] L. K. Eppanapelli, J. Casselgren, J. Wåhlin, and M. Sjödahl, "Investigation of snow single scattering properties based on first order Legendre phase function," *Optics and Lasers in Engineering*, vol. 91, no. July 2016, pp. 151–159, 2017. [Online]. Available: http://dx.doi.org/10.1016/j.optlaseng.2016.11.013

[35] D. H. Male, *The seasonal snowcover*. ACADEMIC PRESS, INC., 1980.

[36] A. Langlois, A. Royer, B. Montpetit, A. Roy, and M. Durocher, "Presenting Snow Grain Size and Shape Distributions in Northern Canada Using a New Photographic Device Allowing 2D and 3D Representation of Snow Grains," *Frontiers in Earth Science*, vol. 7, no. January, 2020.

[37] T. Bartels-Rausch, H. W. Jacobi, T. F. Kahan, J. L. Thomas, E. S. Thomson, J. P. Abbatt, M. Ammann, J. R. Blackford, H. Bluhm, C. Boxe, F. Domine, M. M. Frey, I. Gladich, M. I. Guzmán, D. Heger, T. Huthwelker, P. Klán, W. F. Kuhs, M. H. Kuo, S. Maus, S. G. Moussa, V. F. McNeill, J. T. Newberg, J. B. Pettersson, M. Roeselová, and J. R. Sodeau, "A

review of air-ice chemical and physical interactions (AICI): Liquids, quasi-liquids, and solids in snow," *Atmospheric Chemistry and Physics*, vol. 14, no. 3, pp. 1587–1633, 2014.

[38] J. Luo and Y.-M. Chiang, "Wetting and Prewetting on Ceramic Surfaces," *Annual Review of Materials Research*, vol. 38, no. 1, pp. 227–249, 2008.

[39] J. G. Dash, Haiying Fu, and J. S. Wettlaufer, "The premelting of ice and its environmental consequences," *Reports on Progress in Physics*, vol. 58, no. 1, pp. 115–167, 1995.

[40] R. Rosenberg, "Why is ice slippery?" *Physics Today, American Institute of Physics*, pp. 50–55, 2005.

[41] J. G. Dash, B. L. Mason, and J. S. Wettlaufer, "Theory of charge and mass transfer in ice-ice collisions," *Journal of Geophysical Research*, vol. 106, no. D17, pp. 395–415, 2001.

[42] J. G. Dash, A. W. Rempel, and J. S. Wettlaufer, "The physics of premelted ice and its geophysical consequences," *Reviews of Modern Physics*, vol. 78, no. 3, pp. 695–741, 2006.

[43] E. S. Thomson, "An Optical Study of Ice Grain Boundaries," Ph.D. dissertation, Yale University, 2010.

[44] D. Beaglehole and D. Nason, "Transition layer on the surface on ice," *Surface Science*, vol. 96, no. 1-3, pp. 357–363, 1980.

[45] J. Wåhlin and A. Klein-Paste, "Chemical melting of ice: Effect of solution freezing point on the melting rate," *Transportation Research Record*, vol. 2551, pp. 111–117, 2016.

[46] J. S. Wettlaufer, "Accretion in protoplanetary disks by collisional fusion," *Astrophysical Journal*, vol. 719, no. 1, pp. 540–549, 2010.

[47] R. M. German, "History of sintering: empirical phase," *Powder Metallurgy*, vol. 56, no. 2, pp. 117–123, 2013.

[48] S. C. Colbeck, "A review of sintering in seasonal snow," *CRREL Report*, no. 97-10, p. 12, 1997.

[49] J. R. Blackford, "Sintering and microstructure of ice: A review," *Journal of Physics D: Applied Physics*, vol. 40, no. 21, 2007.

[50] S. Li, J. Marshall, G. Liu, and Q. Yao, "Adhesive particulate flow: The discrete-element method and its application in energy and environmental engineering," *Progress in Energy and Combustion Science*, vol. 37, pp. 633–668, 2011.

[51] M. Higa, M. Arakawa, and N. Maeno, "Size Dependence of Restitution Coefficients of Ice in Relation to Collision Strength," *Icarus*, vol. 133, no. 2, pp. 310–320, 1998.

[52] C. Kloss, C. Goniva, A. Hager, S. Amberger, and S. Pirker, "Models, algorithms and validation for opensource DEM and CFD-DEM," *Progress in Computational Fluid Dynamics, An International Journal*, vol. 12, no. 2/3, p. 140, 2012.

[53] L. Shi, W. Zhao, B. Sun, and W. Sun, "Determination of the coefficient of rolling friction of irregularly shaped maize particles by using discrete element method," *International Journal of Agricultural and Biological Engineering*, vol. 13, no. 2, pp. 15–25, 2020.

[54] C. Dominik and A. G. G. M. Tielens, "The Physics of Dust Coagulation and the Structure of Dust Aggregates in Space," *The Astrophysical Journal*, vol. 480, no. 2, pp. 647–673, 1997.

[55] R. Tamadondar, M, L. de Martín, and A. Rasmuson, "Agglomerate breakage and adhesion upon impact with complex-shaped particles," *AIChE Journal*, no. October 2018, p. e16581, 2019.

[56] L. W. Gold, "Some observations on the dependence of strain on stress for ice," *Canadian Journal of Physics*, vol. 36, no. 1, p. 1265, 1958.

[57] P. V. Hobbs, *Ice Physics*. Oxford University Press, 1974.

[58] B. Gundlach, S. Kilias, E. Beitz, and J. Blum, "Micrometer-sized ice particles for planetary-science experiments â€“ I. Preparation, critical rolling friction force, and specific surface energy," *Icarus*, vol. 214, pp. 717–723, 2011.

[59] M. Vargas, P. M. Struk, R. E. Kreeger, J. Palacios, K. A. Iyer, and R. E. Gold, "Ice particle impacts on a moving wedge," 2013.

[60] J. Y. Tinevez, N. Perry, J. Schindelin, G. M. Hoopes, G. D. Reynolds, E. Laplantine, S. Y. Bednarek, S. L. Shorte, and K. W. Eliceiri, "TrackMate: An open and extensible platform for single-particle tracking," *Methods*, vol. 115, pp. 80–90, 2017.

[61] K. Hashemnia, "Experimental study of the effect of temperature on the coefficient of restitution of steel balls impact to some industrial metal sheets at elevated temperatures," *Powder Technology*, vol. 368, pp. 170–177, 2020.

[62] B. Yildirim, H. Yang, A. Gouldstone, and S. Müftü, "Rebound mechanics of micrometre-scale, spherical particles in high-velocity impacts," *Proceedings of the Royal Society A: Mathematical, Physical and Engineering Sciences*, vol. 473, no. 2204, 2017.

[63] R. B. Bird, W. E. Stewart, and E. N. Lightfoot, *Transport Phenomena*. John Wiley & Sons Inc, 2006.

Appendices

Appendix A

Premelting due to collisional damage

Wettlaufer [46] has established an equation for the predicted liquid layer thickness, d, caused by collisional melting (equation (3.17)). This equation was simplified in Paper II for ice particles colliding with a massive wall by inserting expressions for E_i, a_d and P. The mass of a spherical ice particle is defined as

$$m_p = \rho_s \frac{4}{3}\pi R^3. \tag{A.1}$$

The E_i for a sphere colliding with a stationary wall is

$$E_i = \frac{1}{2} m_p V_i^2 = \rho_s \frac{2}{3}\pi R^3 V_i^2, \tag{A.2}$$

and according to the Hertz contact theory, the maximum contact radius, a_d, is [19]

$$a_d = \Big(\frac{15 m_p R^2 V_i^2}{16 E^*}\Big)^{1/5} = \Big(\frac{5\pi\rho_s V_i^2}{4E^*}\Big)^{1/5} R. \tag{A.3}$$

The contact pressure that causes the damage can be expressed in terms of the maximum contact pressure from Hertz by [46]

$$P = \xi P_d, \tag{A.4}$$

where P_d is the maximum contact pressure from the Hertz contact theory, which is [46]

$$P_d = \frac{3}{2\pi}\Big(\frac{4}{3}\Big)^{4/5}\Big(\frac{5 m_p V_i^2 E^{*4}}{4R^3}\Big)^{1/5}, = \Big(\frac{40}{\pi^4}\rho_s V_i^2 E^{*4}\Big)^{1/5}. \tag{A.5}$$

The liquid layer thickness, d, caused by damage when an ice particle collides with a massive wall can then be expressed as

$$d = \frac{\xi E_i}{\pi a_d^2} \frac{1}{\left(\frac{\rho_l q_m}{T_m}(T_m - T) + \frac{\rho_l - \rho_s}{\rho_s}(P_m - P)\right)}, \tag{A.6}$$

$$= \frac{\xi \rho_s \frac{2}{3} \pi R^3 V_i^2}{\pi \left(\frac{5\pi \rho_s V_i^2}{4E^*}\right)^{2/5} R^2 \left(\frac{\rho_l q_m}{T_m}(T_m - T) + \frac{\rho_l - \rho_s}{\rho_s}(P_m - \xi\left(\frac{40}{\pi^4}\rho_s V_i^2 E^{*4}\right)^{1/5})\right)}, \tag{A.7}$$

$$= \left(\frac{16\sqrt{6}E^*}{135\pi}\right)^{2/5} \frac{\xi R \rho_s^{3/5} V_i^{6/5}}{\left(\frac{\rho_l q_m}{T_m}(T_m - T) + \frac{\rho_l - \rho_s}{\rho_s}\left(P_m - \xi\left(\frac{40}{\pi^4}\rho_s V_i^2 E^{*4}\right)^{1/5}\right)\right)}. \tag{A.8}$$

Papers

PAPER I

Modeling of dry snow adhesion
during normal impact with surfaces

PAPER II

Collisional damping of spherical ice particles